Highly efficient visible-light driven photocatalyst with enhanced charge separation prepared by annealing continuously in ammonia and vacuum

Lei Zeng[a], Zhao Lu[a], Jin Yang[a], Minghui Li[a], Wulin Song[a,b,*], Changsheng Xie[a]

[a] State Key Laboratory of Materials Processing and Die & Mould Technology, Huazhong University of Science and Technology, Luoyu Road No. 1037, Wuhan 430074, PR China
[b] Analytical and testing center, Huazhong University of Science and Technology, Wuhan, PR China

ARTICLE INFO

ABSTRACT

A highly efficient visible light driven photocatalyst was prepared by annealing samples continuously in ammonia and vacuum. The dependence of photocatalytic activity on calcination temperature was investigated. The effect of annealing temperature on crystal structure, particle size, chemical composition and optical absorbance of TiO_2 nanoparticles were characterized by X-ray diffraction, transmission electron microscopy, X-ray photoelectron spectroscopy, photoluminescence spectroscopy and UV–visible diffuse reflectance spectroscopy, respectively. The photocatalytic degradation of benzene under visible light illumination demonstrated that the photocatalyst annealed at 600 °C ($NV-TiO_2$-T600) possessed the best photocatalytic property. The excellent photocatalytic activity of $NV-TiO_2$-T600 was attributed to the high crystallinity, strong light-harvesting and enhanced separation of photo-generated electron–hole pairs. The vacuum treatment had a positive effect on enhancing charge separation. In addition, the increased amount of surface oxygen vacancy might be the crucial factor for the improvement of photocatalytic activity.

© 2014 Elsevier B.V. All rights reserved.

1. Introduction

For decades, TiO_2 has received researchers' enormous attention due to its wide applications in photocatalysis, photonics, sensors and photochromic device [1–4]. Especially for photocatalysis, TiO_2 is recognized as the best choice to purify waste water and eliminate pollutants in atmosphere, since the hydroxyl radicals with powerful oxidization produced in photocatalysis process can oxidize most of the organic pollutants. Unfortunately, the rapid recombination rate of photo-generated electron–hole pairs and the low utilization of the solar spectrum are two major blocks in the practical application of TiO_2 photocatalyst. Hence, many strategies have been developed to step over the aforementioned barriers, including doping, sensitization, coupling with the narrow bandgap semiconductors, introducing carbon nanomaterials and depositing noble metal, etc [5–10]. However, none of these strategies can overcome the two obstacles at the same time. In addition, most of these strategies are complicated and expensive. Thus, it is necessary to prepare a highly efficient photocatalyst by a simple and economical method.

In terms of indoor air pollution, benzene is one of the VOCs (Volatile organic compounds) that can be found everywhere and is carcinogen. Due to the existence of conjugated π bond, benzene is the most stable organic compound [11,12]. Hence, the tough question is how to decompose benzene completely. Among the technologies developed for treatment of benzene, the photocatalytic oxidation process is considered to be a promising technology due to the •OH radicals with strong oxidizing capability which could oxidize most of organic compounds generate in the process. A series of related studies have been carried out in the past few years. Zhong et al. have investigated the photocatalytic property of Pd/TiO_2 for the oxidation of gaseous benzene. They find the optimal ratio of Pd/Ti and the maximum conversion of benzene (initial concentration is 4.5 ppm), which is 65.3% after 6 h exposure to UV light [13]. Wang et al. have prepared novel TiO_2/Ag_3VO_4 nanocomposite photocatalyst. The photo-degradation results show that the conversion of benzene (initial concentration is 280 ppm) on 0.5% AT can reach 95% and the mineralization ratio is up to 84% under 10 h of visible light illumination [14]. However, these efforts are not sufficient to

* Corresponding author at: State Key Laboratory of Materials Processing and Die & Mould Technology, Huazhong University of Science and Technology, Luoyu Road No. 1037, Wuhan 430074, PR China. Tel.: +86 27 87557453; fax: +86 27 87557453.
E-mail address: wulins@126.com (W. Song).

solve some remained problems, such as long reaction duration, low initial concentration of benzene, high dosage of photocatalyst and expensive cost of production.

Vacuum treatment is an effective and economical technology to modify the surface of materials. Xing et al. have reported a photocatalyst with high photo-activity and photosensitivity prepared by a vacuum activated procedure and suggested that the oxygen vacancy states together with the Ti^{3+} were responsible for the high yield of H_2 [15]. Luo et al. have investigated the photocatalytic activity of TiO_2 annealed in reducing atmosphere. They believe that the excellent photocatalytic activity of vacuum-activated TiO_2 may be related to subnanometer-thick disordered surface layers [16]. Therefore, we can conclude that vacuum treatment can efficiently improve the photocatalytic activity of TiO_2.

In the present work, we prepare a modified TiO_2 with high visible light photocatalytic activity by annealing continuously in ammonia and vacuum. To our surprise, this method not only makes TiO_2 respond to visible light but also enhances the separation of photo-generated electron–hole pairs. To our best knowledge, it is the first time to use an economical and simple method to achieve the two goals simultaneously. In addition, the activities of photocatalysts and their dependence on annealing temperature are also compared. It is heartening that the as-prepared photocatalyst annealed at 600 °C (NV-TiO_2-T600) can decompose high concentration of gaseous benzene (300 ppm) during 4 h of visible light illumination. The excellent photocatalytic activity may be ascribed to the high crystallinity, strong light-harvesting and fast separation of electron–hole pairs. Our findings provide an economical and convenient method to prepare highly efficient visible light driven photocatalyst.

2. Experimental

2.1. Synthesis of NV-TiO_2-Tx

The pure TiO_2 was synthesized by hydrothermal method mentioned in previous paper [17]. Then the pure TiO_2 was transferred into tube furnace and annealed in ammonia (99.9%) for 2 h. After that, ammonia stopped inletting and the vacuum pump opened immediately. The vacuum treatment lasted for 2 h, followed by naturally cooling to room temperature in vacuum (vacuum degree −0.1 atm). The heating rate was 5 °C/min. The annealing temperature ranged from 550 to 750 °C. The as-prepared sample was denoted as NV-TiO_2-Tx (x referred to the annealing temperature). The pure TiO_2 only annealed in ammonia at 600 °C for 2 h was denoted as N-TiO_2-T600.

2.2. Characterization

The crystal phases of samples were analyzed by X-ray diffraction with Cu Kα radiation (XRD: PANalytical B.V., Almelo, Netherlands). The morphology, structure and grain size of the samples were examined by transmission electron microscopy (TEM: FEI Tecnai G2 F30, Netherlands). XPS with Al Kα X-rays radiation operated at 300 W (XPS: Kratos XSAM800 spectrometer, USA) was used to analyze the surface properties. The shift of binding energy due to relative surface charging was corrected using the C 1s level at 284.6 eV as an internal standard. The spectra were fitted using a nonlinear least-squares fitting program (XPSPEAK) with a linear background and to the 80% Gausssian/20% Lorentzian peak shape. The PL spectra were gained by using a LabRAM HR spectrometer (HORIBA Jobin Yvon, France) with a laser excitation of 325 nm. The UV–vis absorbance spectra were obtained for the dry-pressed disk samples using a Scan UV–vis spectrophotometer (Perkin-Elmer, Lambda 950) equipped with an integrating sphere assembly. The spectra were recorded at room temperature in air within the range 200–900 nm.

2.3. Measurement of photocatalytic activity

Evolution of the photocatalysis was carried out in a self-designed closed aluminum alloy reactor. The volume of reactor is 2 L. The mass of photocatalyst was 0.10 g and well dispersed to form a thin layer over an aluminum slice (50 mm × 50 mm). The initial concentration of benzene was kept at 300 ppm for all experiments. The concentration of benzene was monitored every 10 min by GC 9560 gas-phase chromatogram equipped with FID detector. A 300 W Xe lamp was put over the reactor to irradiate the samples. For the visible light, an appropriate filter which cuts off the wavelength below 400 nm was placed on top of the reactor to remove the ultraviolet radiation from the lamp. The conversion was calculated by $(C_0 − C)/C_0$, where C is the concentration of the reactant after irradiation, C_0 is the concentration of the reactant after adsorption equilibrium but before the irradiation in the presence of catalyst.

3. Results and discussion

3.1. Photocatalytic activity test

The photo-degradation of benzene on surface of NV-TiO_2-Tx under visible light illumination is compared in Fig. 1. It is obvious to see that NV-TiO_2-T600 possesses the best photocatalytic activity. The conversion of benzene reaches 95.2% after 4 h of visible
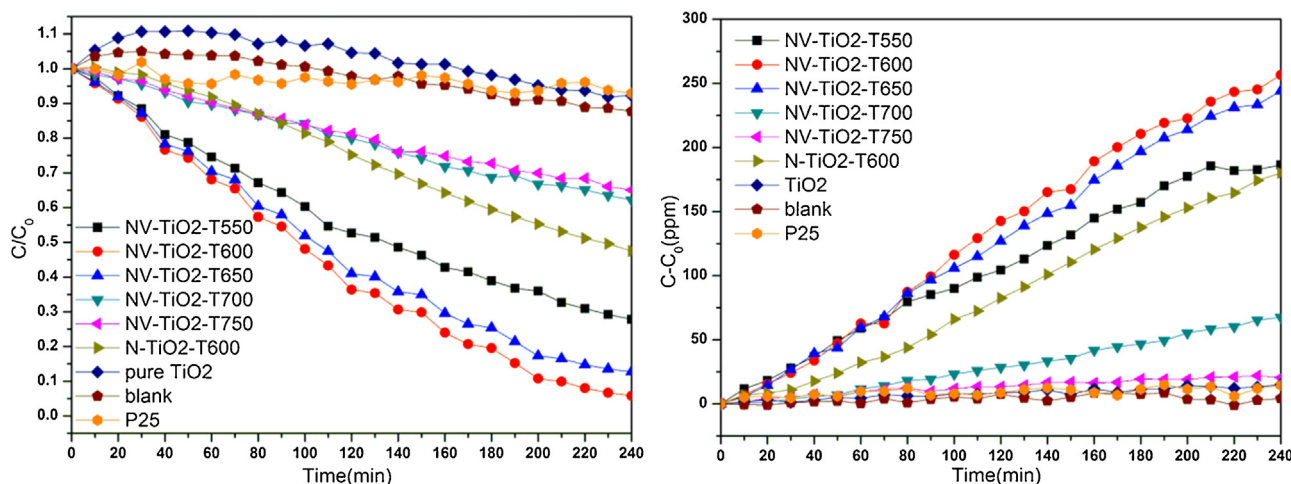

Fig. 1. Catalytic degradation of benzene (left) and CO_2 generation (right) by using all samples under visible light illumination.

light illumination. The other samples apparently present much worse photocatalytic activity. In the contrast group, we add no photocatalyst or only employ equal amounts of P25 photocatalyst. The concentration of benzene has not decreased obviously, indicating that benzene is stable under visible light illumination and the airtightness of self-designed test platform is well enough. In addition, it implies that P25 photocatalyst has no visible light photocatalytic ability. With regard to these distinctions, the excellent photocatalytic activity of NV-TiO$_2$-T600 will be proposed base on the following analysis.

3.2. Microstructure and phase

3.2.1. XRD characterization

XRD was widely used to analyze the crystal structure, phase composition, and grain size of the prepared samples and the effect of doping and heating temperature on grain size and crystal phase. Fig. 2 shows the XRD patterns of pure TiO$_2$ and NV-TiO$_2$-Tx samples. From Fig. 2, it is evident that the pure TiO$_2$ consists of anatase (JCPDS file No. 21-1272) and brookite (JCPDS file No. 03-0380). In addition, the peak intensity is weak and the shape of peaks is not intact in the pure TiO$_2$ sample, indicating that the crystallinity of pure TiO$_2$ is poor. It also can be seen that the NV-TiO$_2$-Tx sample exists in anatase phase and brookite phase up to 650 °C, and it starts rutilization at 700 °C as evidenced by the appearance of a diffraction peak at around 27.5° as well as the absolute disappearance of brookite phase. When annealing temperature rises to 750 °C, the NV-TiO$_2$-T750 sample only exists in rutile phase (JCPDS file No. 21-1276).
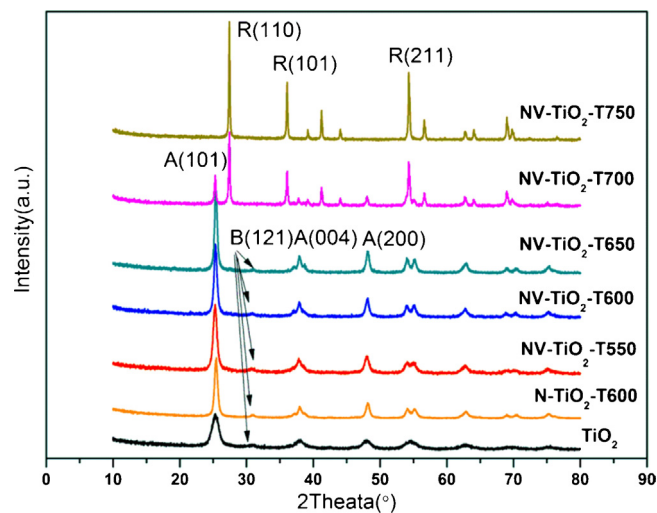

Fig. 2. XRD patterns for pure TiO$_2$, NV-TiO$_2$-T550, NV-TiO$_2$-T600, NV-TiO$_2$-T650, NV-TiO$_2$-T700 and NV-TiO$_2$-T750.

Compared to that of pure TiO$_2$, the crystallinity of NV-TiO$_2$-Tx samples has been improved. The changes of crystallinity and crystalline size for all samples are estimated by profile fitting the strongest XRD peak (using XRD analysis software-X'pert high score plus) and the results are listed in Table 1. It is clear from data that the average grain size and the crystallinity of all samples increase moderately
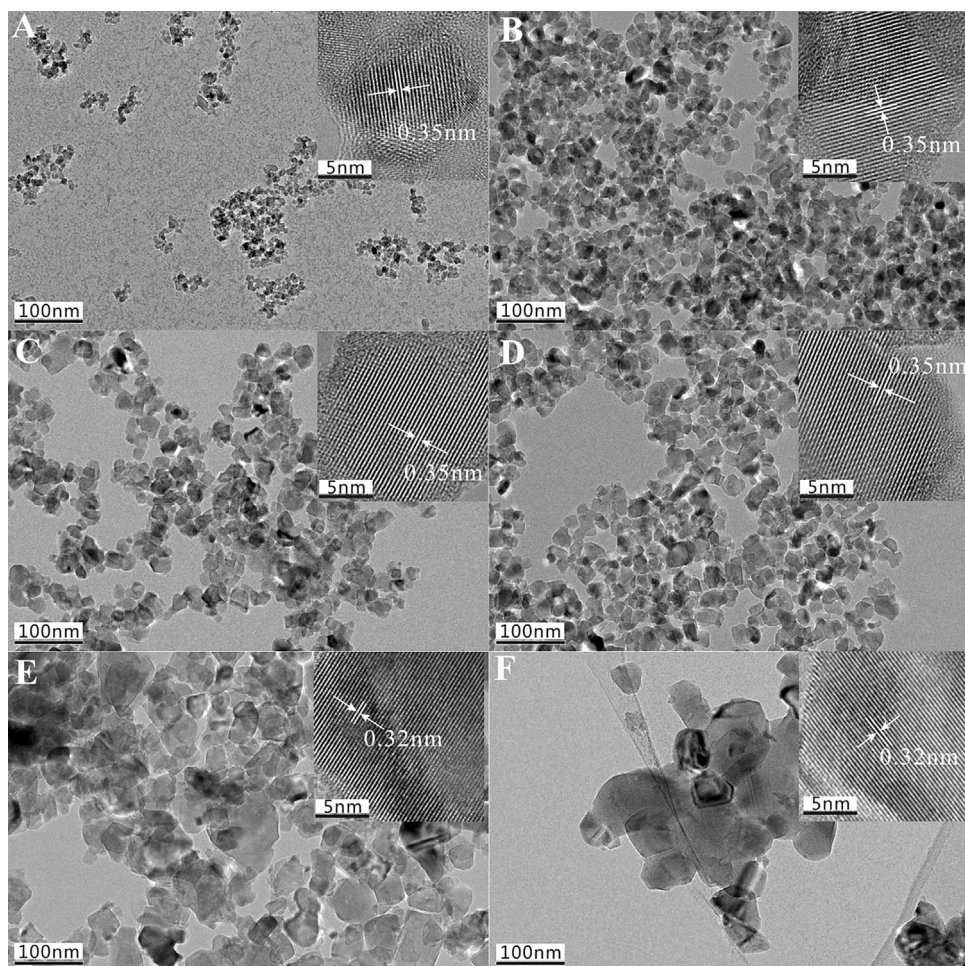

Fig. 3. TEM images of (A) pure TiO$_2$, (B) NV-TiO$_2$-T550, (C) NV-TiO$_2$-T600, (D) NV-TiO$_2$-T650, (E) NV-TiO$_2$-T700 and (F) NV-TiO$_2$-T750.

Table 1
Data for all samples from XRD and XPS O_L: O 1s core level peak at ca. 529.9 eV for TiO_2 O_C: O 1s core level peak at ca. 530.4 eV for TiO_2 O_H: O 1s core level peak at ca. 531.6 eV for TiO_2.

sample	Crystalline size(nm)	Crystallinit%	Nitrogen mass concentration%	O_H/O_L	O_C/O_L	Eg (eV)
Pure TiO_2	11.1	50	–	0.80	2.08	3.12
NV-TiO_2-T550	19.5	55.17	0.43	0.71	2.76	2.81
NV-TiO_2-T600	28.1	78.29	0.40	0.65	2.55	2.58
NV-TiO_2-T650	49.4	76.11	0.50	0.54	1.88	2.86
NV-TiO_2-T700	57.6	61.86	0.37	0.41	1.43	2.66
NV-TiO_2-T750	108.7	65.24	0.39	0.35	1.01	2.90
N-TiO_2-T600	27.2	63.92	0.31	0.31	1.41	2.61

with increasing calcination temperature. The variation in the grain size and the phase composition demonstrates that the annealing in ammonia and vacuum can suppress grain growth and retard the disappearance of brookite and phase transformation from anatase to rutile, which is in accord with previous publications [18,19].

3.2.2. TEM characterization

As shown in Fig. 3, the particle size of all samples can be directly compared since each image is shown with the same scale bar. It is evident that the pure TiO_2 and the samples annealed from 550 °C to 650 °C possess good dispersibility. When annealing temperature rises to 700 °C, the particles aggregate and grow further. For NV-TiO_2-T750 sample, the particles are agglomerated severely. Further information on the samples is obtained by their high resolution TEM images and shown in the inset of Fig. 3. The fringe of $d = 0.35$ nm is observed in pure TiO_2 and the samples annealed from 550 °C to 650 °C matches (1 0 1) crystallographic planes of anatase TiO_2. The fringe of $d = 0.32$ nm corresponded to the (1 1 0) crystallographic planes of rutile TiO_2 is observed in NV-TiO_2-T700 and NV-TiO_2-T750 samples, which is in good agreement with the XRD results.

3.3. Chemical composition

XPS analyses are carried out to determine the composition of all samples and identify the valence state of various species present herein. The N 1s peak of all as-prepared samples is exhibited in Fig. 4. It is evident that the samples annealed in ammonia and vacuum from 550 °C to 750 °C appear only one N 1s peak located at 400.3 eV which is usually ascribed to the interstitial nitrogen species. However, three kinds of surface nitrogen species are present in N-TiO_2-T600. The first peak at 396.1 eV is assigned to the substitutional nitrogen dopant due to the N 1s peak at 395.6 eV is characteristic of N^{3-} that corresponds to TiN. The N 1s peak at

395–397 eV obtained from N-doped TiO_2 has also been assigned to the Ti–N bonding by other researchers [20–23]. The second peak at 400 eV is typically assigned to the interstitial nitrogen dopant which was summarized by Fujishima et al. [24]. The last peak locates at 403.6 eV can be assigned to the NO_x. In the previous publications [25], the location of nitrogen dopant in the lattice of TiO_2 varied with the heating temperature for the samples annealed in ammonia. However, in the present work, the nitrogen doping sites remain unchanged with the rise of annealing temperature, implying that the vacuum treatment can inhibit the formation of substitutional nitrogen species. The concentrations of nitrogen dopants in all samples are similar and listed in Table 1, implying that the photocatalytic activity is irrelevant to the concentration of nitrogen dopant in our investigation.

The difference between the values of Ti 2p3/2 and Ti 2p1/2 is always used to identify the valence of Ti element in modified TiO_2. Herein, the XPS spectra have a split of 5.7 eV between Ti 2p3/2 and Ti 2p1/2 for all samples, indicating that Ti exists in the form of Ti^{4+} [26–28]. To our surprise, there are no signals related to Ti^{3+}. This observation demonstrates that the surfaces of all samples are dominated by Ti^{4+}. The O 1s XPS spectra for all samples can be fitted into three peaks in Fig. 5. The peak belonging to lattice oxygen atoms locates at 529.9 eV (labeled as O_L), the peak at 531.6 eV is assigned to surface hydroxyl oxygen (labeled as O_H), and the third peak at around 530.4 eV is ascribed to chemisorbed O_2 (labeled as O_C) [29–31]. O_H/O_L ratios on surface of samples estimated from XPS spectra are given in Table 1. The O_H/O_L ratio of pure TiO_2 is the highest and decreases obviously with increasing annealing temperature, indicating that the concentration of hydroxyl group decreases and the crystallinity is enhanced since the ratio of O_L in oxygen atoms increases gradually.

3.4. Optical property

3.4.1. UV–visible diffuse reflection spectrum

Fig. 6 shows the UV–visible spectra for pure TiO_2 and modified TiO_2. Comparing to the pure TiO_2, the significant red-shift of absorption edge occurs in modified TiO_2, and the N-TiO_2-T600 sample has the largest red-shift and displays a typical absorption region between 400 nm and 550 nm. According to Kubelka–Munk equation, the transformation of UV–visible spectrum is exhibited in the right of Fig. 6 and the band gap energy (Eg) of all samples are listed in Table 1. From the data in Table 1, it is apparently that the band gap of modified TiO_2 has reduced comparing to pure TiO_2. It suggests that the N atoms have incorporated into the lattice of TiO_2 successfully after annealing treatment. More importantly, the band gap of NV-TiO_2-T600 is narrower than that of N-TiO_2-T600, indicating that more energy levels may be generated or the shift of energy level is occurred after vacuum treatment.

3.4.2. PL spectra

The efficiency of charge carriers trapping, migration and transfer was usually detected by PL emission spectra. In addition, the variation of PL intensity may result from the change of defect state
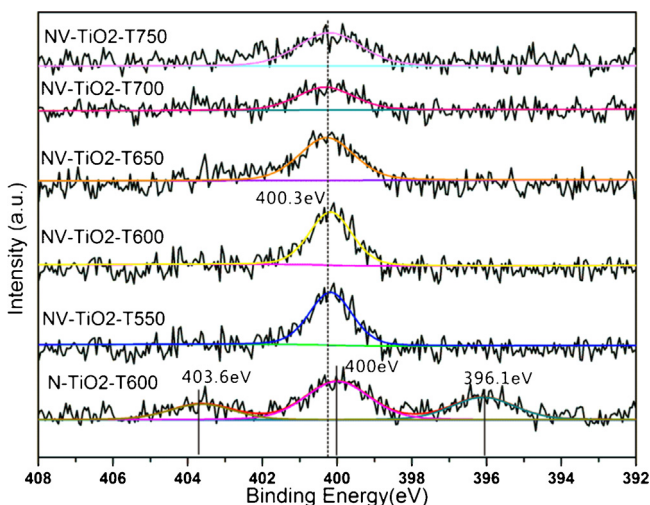

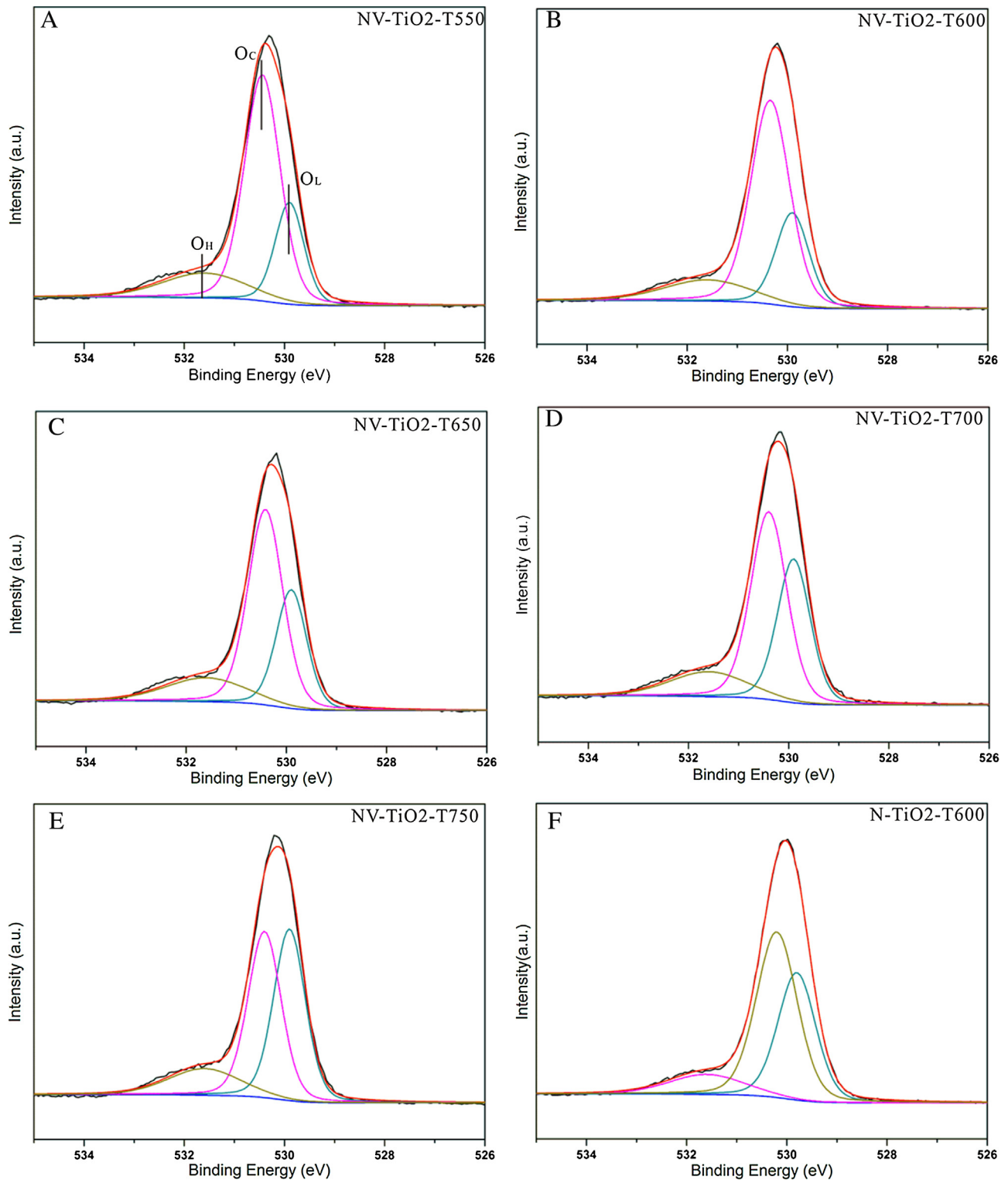**Fig. 4.** N 1s XPS spectra for all modified samples.

Fig. 5. O 1s XPS spectra for all modified samples.

on the shallow level of the measured material surface. The difference of PL spectra in Fig. 7 is due to the different phase structure and surface state brought by various calcination temperatures. The highest PL emission intensity is presented in the NV-TiO$_2$-T700 sample, indicating that the recombination of electron–hole pairs is the most severe. It may be ascribed to the co-existence of anatase and rutile in NV-TiO$_2$-T700 sample. The recombination of charge carriers usually occurs at the grain boundary of two phases. With

decreasing calcination temperature, there is a significant decrease in the intensity of PL spectra. Meanwhile, the NV-TiO$_2$-T750 sample has the weakest PL signal and it may be attributed to the existence of high crystalline rutile. Compared to N-TiO$_2$-T600, the PL intensity of NV-TiO$_2$-T600 weakens significantly, implying the decrease in recombination rate. More importantly, the main peak shifts toward short wavelength direction compared with pure TiO$_2$, indicating that the energy band structure has been changed after annealing
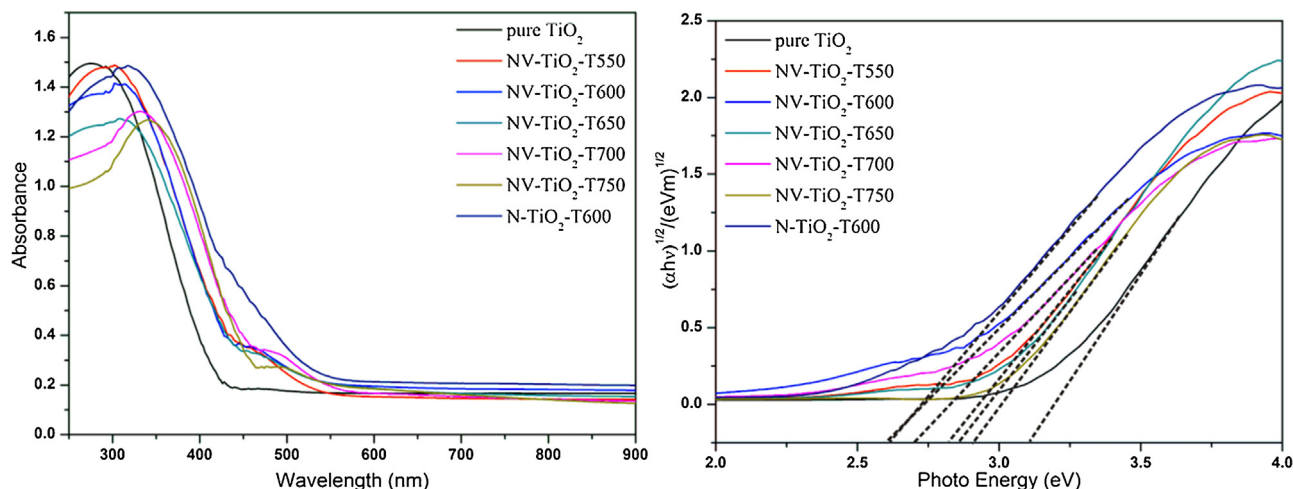
Fig. 6. UV–vis DRS and Kubelka–Munk transformation of the spectrum for all samples.

in ammonia. The deconvolution of PL spectrum for pure TiO_2, N-TiO_2-T600 and NV-TiO_2-T600 is also shown in Fig. 7. It is evident to see that the PL spectrum of pure TiO_2 can be divided into four peaks centered at about 1.83 eV, 2.12 eV, 2.4 eV and 2.71 eV, which are attributed to self-trapped excitons located at TiO_6 actahedra, the Ti interstitial, the oxygen vacancy with one trapped electrons

(V_{O1}) and the oxygen vacancy with two electrons (V_{O2}), respectively [32–34]. For N-TiO_2-T600 sample, the peak located at 1.89 eV is ascribed to the electron transition from energy level of V_{O1} to interstitial nitrogen. The electron transition from energy level of V_{O1} to substitutional nitrogen is responsible for the peak centered at 2.26 eV. The peak located at 2.61 eV is assigned to the emission
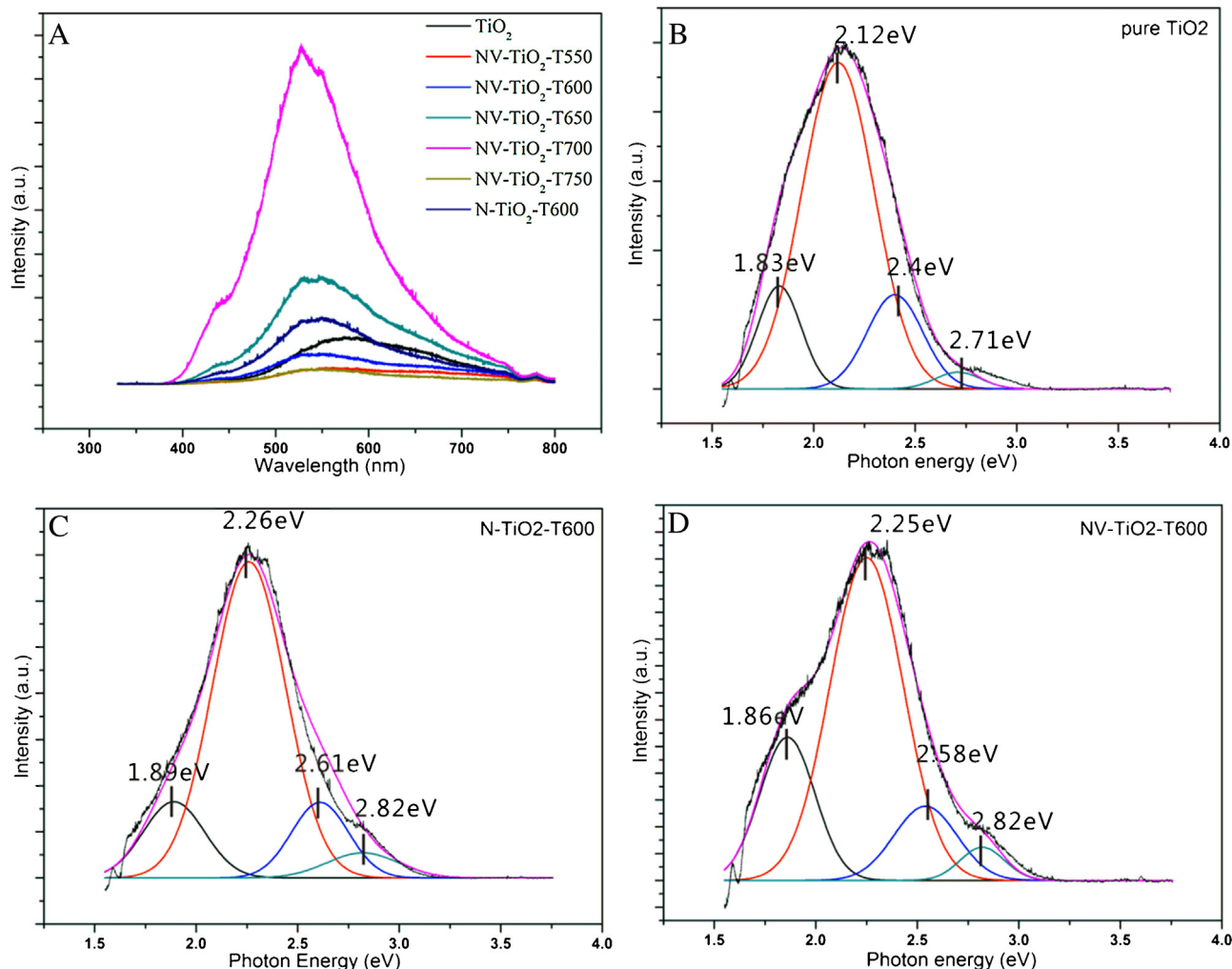

Fig. 7. PL spectra of all samples and the deconvolution of PL spectrum for pure TiO_2, N-TiO_2-T600 and NV-TiO_2-T600.
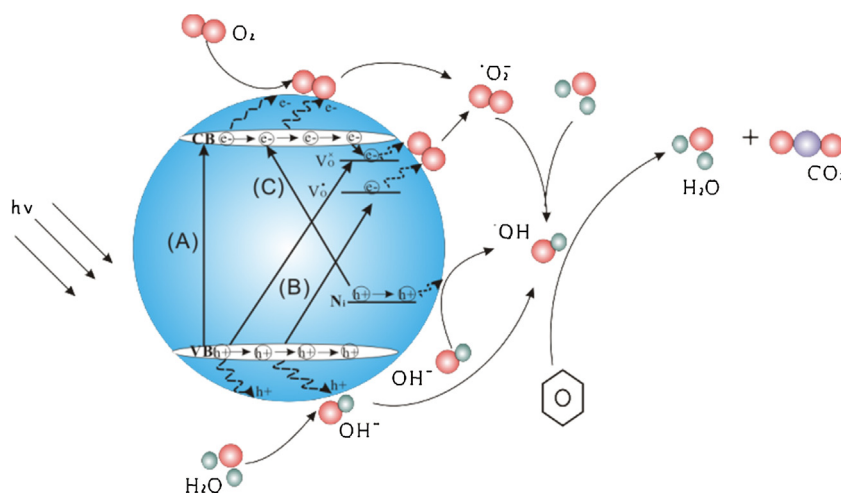
Fig. 8. Schematic diagram for the band structure of NV-TiO$_2$-T600 and the photocatalytic mechanism.

from the transition between conduction band and interstitial nitrogen. The last peak at 2.82 eV may be attributed to the presence of hydroxyl species which may form an acceptor level just above the valence band. After vacuum treatment, the main peak shift toward low energy direction slightly. The peak at 1.86 eV is assigned to the electron transition between V_{O1} and interstitial nitrogen. The peak located at 2.25 eV is ascribed to the electron transition from energy level of V_{O2} to interstitial nitrogen. The peak centered at 2.58 eV is attributed to the transition from conduction band to interstitial nitrogen energy level.

3.5. Discussion

The nitrogen doping mechanism of TiO$_2$ has been investigated extensively. It has been reported that the doped N would exist as interstitial nitrogen dopant, substitutional nitrogen dopant and N–O$_x$ surface species in N-doped TiO$_2$, for which the energy level located at 0.73 eV, 0.14 eV and 0.25 eV above the valence band of TiO$_2$, respectively [35–39]. The existence of nitrogen dopant can effectively reduce the band gap of TiO$_2$ thereby making TiO$_2$ sensitizes to visible light. At the same time, the different types of nitrogen dopants play different roles. For maximum reduction of band gap, interstitial nitrogen doping is the best strategy. However, the deep energy level of interstitial nitrogen dopant in band gap tends to be the recombination center of electron–hole pairs. For substitutional nitrogen doping, the visible light response arise from occupied N 2p localized state mixed with O 2p state. Hence, the reduction of band gap in substitutional nitrogen doped TiO$_2$ cannot be compared with that in interstitial nitrogen doped TiO$_2$. For the modification of TiO$_2$ by N–O$_x$ surface species, the electron excitation to conduction band from energy level of N–O$_x$ surface species in N-doped TiO$_2$ is responsible for its visible light response. Moreover, the recombination of photo-generated charge carriers would be inhibited since the energy level of N–O$_x$ surface species act as hole trapping centers [40].

In terms of energy, nitrogen atoms favor to occupy interstitial site. After nitrogen atoms at interstitial site become saturated, excessive nitrogen atoms will incorporate into substitutional sites [41]. For vacuum treatment, oxygen atoms leave the lattice and oxygen vacancies form. Hence, the substitutional nitrogen atoms escape from the lattice and enter into the interstitial position. In this work, the nitrogen atoms incorporate into the interstitial sites of TiO$_2$ lattice for all vacuum treated samples. However, NV-TiO$_2$-T600 photocatalyst shows much weaker recombination of electron–hole pairs than N-TiO$_2$-T600, which is confirmed by PL

spectra. That may be ascribed to delocalized electrons trapped by oxygen vacancies.

Based on aforementioned analysis, the highly visible-light photocatalytic activity of NV-TiO$_2$-T600 is mainly related to the continuous annealing of TiO$_2$ in ammonia and vacuum. The explanation will focus on the difference of photocatalytic activity among pure TiO$_2$, N-TiO$_2$-T600 and NV-TiO$_2$-T600. The worse photocatalytic activity of other four samples is ascribed to the poorer crystallinity and stronger recombination of charge carriers. For pure TiO$_2$, the band to band transition hardly occurs since it cannot respond to visible light (process A). Its large band gap (3.12 eV) is deduced by the Kubelka–Munk transformation of UV–vis DRS spectrum and it is close to theoretical value (3.2 eV). For N-TiO$_2$-T600, the nitrogen atoms incorporate into the substitutional sites and interstitial sites of TiO$_2$ lattice, which is confirmed by XPS characterization. The interstitial nitrogen impurity energy level trend to be the recombination center of photoinduced charge carriers, the photocatalytic activity has been weaken at some extent. Compared with N-TiO$_2$-T600, the surface of NV-TiO$_2$-T600 after vacuum treatment has been activated due to the introduction of oxygen vacancies, as shown in Fig. 8. The oxygen vacancy always acts as electron trapping center, and the atoms closed to oxygen vacancies commonly play the role of reaction centers (active sites) [42–44]. The photo-generated electrons from conduction band and energy level of oxygen vacancies can be captured directly by the adsorbed O$_2$ molecules (electron scavenger) on the surface of NV-TiO$_2$-T600 to form active species and then further transform to •OH radicals (process B) [43,45]. Meanwhile, the photogenerated holes injected by valence band and generated at the energy level of interstitial nitrogen dopants can directly oxidize benzene or oxidize the surface hydroxyl groups to form •OH radicals that can further decompose benzene (process C). In short, the oxygen vacancy induced by vacuum treatment could trap electrons to accelerate separation of charge carries. Hence, gaseous benzene can be decomposed by two paths in NV-TiO$_2$-T600. In addition, the highly crystallized grains provide channels for charge carriers transferring from bulk to surface immediately and the high ratio of surface hydroxyl groups provide abundant precursors for the formation of •OH radicals with strong oxidation which are also responsible for the excellent photocatalytic activity of NV-TiO$_2$-T600.

4. Conclusions

A highly efficient visible light driven photocatalyst NV-TiO$_2$-T600 has been successfully prepared by continuous annealing in

ammonia and vacuum. The simple annealing method empowers TiO$_2$ the ability to respond to visible light and simultaneously enhance the separation of photogenerated electron–hole pairs. Through a series of characterization and analysis, the improvement of photocatalytic activity can be ascribed to the combined impact of high crystallinity, strong light-harvesting, fast separation rate of photogenerated charge carriers and increased amount of active sites induced by oxygen vacancy. Our findings provide a convenient and economical strategy to industrial-scale production of photocatalyst with high visible light driven photocatalytic activity. Meanwhile, it aids us to deepen the understanding of the effect of vacuum treatment on the photocatalytic property.

Acknowledgement

References

[1] R. Asahi, T. Morikawa, T. Ohwaki, K. Aoki, Y. Taga, Science 293 (2001) 269–271.
[2] R.A. Caruso, A. Susha, F. Caruso, Chem. Mater. 13 (2001) 400–409.
[3] Y.F. Zhu, J.J. Shi, Z.Y. Zhang, C. Zhang, X.R. Zhang, Anal. Chem. 74 (2002) 120–124.
[4] K. Naoi, Y. Ohko, T. Tatsuma, J. Am. Chem. Soc. 126 (2004) 3664–3668.
[5] D.M. Chen, Z.Y. Jiang, J.Q. Geng, Q. Wang, D. Yang, Ind. Eng. Chem. Res. 46 (2007) 2741–2746.
[6] L.C. Liu, X.R. Gu, Y. Cao, X.J. Yao, L. Zhang, C.J. Tang, F. Gao, L. Dong, ACS Catal. 3 (2013) 2768–2775.
[7] X.Z. Li, F.B. Li, C.L. Yang, W.K. Ge, J. Photochem. Photobiol. A: Chem. 141 (2001) 209–217.
[8] W.T. Sun, Y. Yu, H.Y. Pan, X.F. Gao, Q. Chen, L.M. Peng, J. Am. Chem. Soc. 130 (2008) 1124–1125.
[9] G. Williams, B. Seger, P.V. Kamat, ACS Nano 2 (2008) 1487–1491.
[10] D.H. Wang, D.W. Choi, J. Li, Z.G. Yang, Z.M. Nie, R. Kou, D.H. Hu, C.M. Wang, L.V. Saraf, J.G. Zhang, I.A. Aksay, J. Liu, ACS Nano 3 (2009) 907–914.
[11] J.X. Wang, H. Ruan, W.J. Li, D.Z. Li, Y. Hu, J. Chen, Y. Shao, Y. Zheng, J. Phys. Chem. C 116 (2012) 13935.
[12] H.H. Kim, S.M. Oh, A. Ogata, S. Futamura, Appl. Catal. B: Environ. 56 (2005) 213.
[13] J.B. Zhong, Y. Lu, W.D. Jiang, Q.M. Meng, X.Y. He, J.Z. Li, Y.Q. Chen, J. Hazard. Mater. 168 (2009) 1632–1635.
[14] J.X. Wang, H. Ruan, W.J. Li, D.Z. Li, Y. Hu, J. Chen, Y. Shao, Y. Zheng, J. Phys. Chem. C 116 (2012) 13935–13943.
[15] M.Y. Xing, J.L. Zhang, F. Chen, B.Z. Tian, Chem. Commun. 47 (2011) 4947–4949.
[16] M. Samiee, J. Luo, Mater. Lett. 98 (2013) 205–208.
[17] H.Y. Li, D.J. Wang, H.M. Fan, P. Wang, T.F. Jiang, T.F. Xie, J. Colloid Interface Sci. 354 (2011) 175–180.
[18] G. Liu, F. Li, Z.G. Chen, G.Q. Lu, H.M. Cheng, J. Solid State Chem. 179 (2006) 331–335.
[19] H.Y. Chen, A. Nambu, W. Wen, J. Graciani, Z. Zhong, J.C. Hanson, E. Fujita, J.A. Rodriguez, J. Phys. Chem. C 111 (2007) 1366–1372.
[20] M. Sathish, B. Viswanathan, R.P. Viswanath, C.S. Gopinath, Chem. Mater. 17 (2005) 6349–6353.
[21] X.B. Chen, C. Burda, J. Phys. Chem. B 108 (2004) 15446–15449.
[22] M.S. Wong, H.P. Chou, T.S. Yang, Thin Solid Films 494 (2006) 244–249.
[23] S. Sakthivel, M. Janczarek, H. Kisch, J. Phys. Chem. B 108 (2004) 19384–19387.
[24] A. Fujishima, X. Zhang, D. Tryk, Surf. Sci. Rep. 63 (2008) 515–585.
[25] J. Wang, D.N. Tafen, J.P. Lewis, Z.L. Hong, A. Manivannan, M.J. Zhi, M. Li, N.Q. Wu, J. Am. Chem. Soc. 131 (2009) 12290–12297.
[26] T.C. Jagadale, S.P. Takale, R.S. Sonawane, H.M. Joshi, S.I. Patil, B.B. Kale, S.B. Ogale, J. Phys. Chem. C 112 (2008) 14595–14602.
[27] Z.Z. Zhang, X.X. Wang, J.L. Long, Q. Gu, Z.X. Ding, X.Z. Fu, J. Catal. 276 (2010) 201–214.
[28] C.X. Feng, Y. Wang, Z.S. Jin, J.W. Zhang, S.L. Zhang, Z.S. Wu, Z.J. Zhang, New J. Chem. 32 (2008) 1038–1047.
[29] L. Zeng, W.L. Song, M.H. Li, D.W. Zeng, C.S. Xie, Appl. Catal. B: Environ. 147 (2014) 490–498.
[30] Z.Z. Zhang, J.L. Long, X.Q. Xie, H.Q. Zhuang, Y.G. Zhou, H. Lin, R.S. Yuan, W.X. Dai, Z.X. Ding, X.X. Wang, X.Z. Fu, Appl. Catal. A: Gen. 425 (2012) 117–124.
[31] Y. Liu, Q. Yang, J.H. Wei, R. Xiong, C.X. Pan, J. Shi, Mater. Chem. Phys. 129 (2011) 654–659.
[32] W.F. Zhang, M.S. Zhang, Z. Yin, Q. Chen, Appl. Phys. B 70 (2000) 261.
[33] J. Buha, Thin Solid Films 545 (2013) 234.
[34] B. Santara, P.K. Giri, K. Imakita, M. Fujii, J. Phys. Chem. C 117 (2013) 23402.
[35] S. Livraghi, M.C. Paganini, E. Giamello, A. Selloni, C.D. Valentin, G. Pacchioni, J. Am. Chem. Soc. 128 (2006) 15666–15671.
[36] C.D. Valentin, G. Pacchioni, A. Selloni, S. Livraghi, E. Giamello, J. Phys. Chem. B 109 (2005) 11414–11419.
[37] C.D. Valentin, E. Finazzi, G. Pacchioni, A. Selloni, S. Livraghi, M.C. Paganini, E. Giamello, Chem. Phys. 339 (2007) 44–56.
[38] C.D. Valentin, G. Pacchioni, A. Selloni, Phys. Rev. B 70 (2004) 85116–85120.
[39] M.A. Henderson, W.S. Epling, C.H.F. Peden, C.L. Perkins, J. Phys. Chem. B 107 (2003) 534–545.
[40] Y.Q. Cao, Y.L. Yu, P. Zhang, L.L. Zhang, T. He, Y.A. Cao, Sep. Purif. Technol. 104 (2013) 256–262.
[41] J. Wang, D.N. Tafen, J.P. Lewis, Z.L. Hong, A. Manivannan, M.J. Zhi, N.Q. Wu, J. Am. Chem. Soc. 131 (2009) 12290–12297.
[42] W. Zhao, Q. Zhong, Y.X. Pan, R. Zhang, Colloid Surf. A 436 (2013) 1013–1020.
[43] H.F. Li, N. Zhang, P. Chen, M.F. Luo, J.Q. Lu, Appl. Catal. B: Environ. 110 (2011) 279–285.
[44] Z.F. Zheng, J. Teo, X. Chen, H.W. Liu, Y. Yuan, E.R. Waclawik, Z.Y. Zhong, H.Y. Zhu, Chem. Eur. J. 16 (2010) 1202–1211.
[45] J.B. Zhong, J.L. Wang, L. Tao, M.C. Gong, Z.M. Liu, Y.Q. Chen, J. Hazard. Mater. 139 (2007) 323–331.